math xmlns="http://www.w3.org/1998/Math/MathML">mi>A/mi>/math>-type antiferromagnetic order in the Zintl-phase insulator math xmlns="http://www.w3.org/1998/Math/MathML">mrow>msub>mi>EuZn/mi>mn>2/mn>/msub>msub>mi mathvariant="normal">P/mi>mn>2/mn>/msub>/mrow>/math>

Tanya Berry, Veronica J. Stewart, Benjamin W. Y. Redemann, Chris Lygouras, Nicodemos Varnava, David Vanderbilt, and Tyrel M. McQueen

Phys. Rev. B **106**, 054420 — Published 17 August 2022
DOI: 10.1103/PhysRevB.106.054420

A-type Antiferromagnetic Order in the Zintl Phase Insulator $EuZn_2P_2$

Tanya Berry,[1,2*] Veronica J. Stewart,[1,2] Benjamin W. Y. Redemann,[1,2] Chris Lygouras,[2] Nicodemos Varnava,[3] David Vanderbilt,[3] Tyrel M. McQueen[1,2,4**]

[1]Department of Chemistry, Johns Hopkins University, Baltimore, Maryland 21218, USA

[2]Institute for Quantum Matter, William H. Miller III Department of Physics and Astronomy, Johns Hopkins University, Baltimore, Maryland 21218, USA

[3]Department of Physics & Astronomy, Rutgers University, Piscataway, New Jersey 08854, USA

[4]Department of Materials Science and Engineering, Johns Hopkins University, Baltimore, Maryland 21218, USA

* Email: tberry@ucdavis.edu and **Email: mcqueen@jhu.edu

Abstract: Zintl phases, containing strongly covalently bonded frameworks with separate ionically bonded ions, have emerged as a critical materials family in which to couple magnetism and strong spin orbit coupling to drive diverse topological phases of matter. Here we report the single-crystal synthesis, magnetic, thermodynamic, transport, and theoretical properties of the Zintl compound $EuZn_2P_2$ that crystallizes in the anti-La_2O_3 ($CaAl_2Si_2$) P-3m1 structure, containing triangular layers of Eu^{2+} ions. In-plane resistivity measurements reveal insulating behavior with an estimated activation energy of E_g=0.11eV. Specific heat and magnetization measurements indicate antiferromagnetic ordering at T_N=23 K. Curie-Weiss analysis of in-plane and out-of-plane magnetic susceptibility from T=150-300K yields p_{eff}=8.61 for $\mu_0 H \perp c$ and p_{eff}=7.74 for $\mu_0 H // c$ close to the expected values for the $4f^7$ $J=S=7/2$ Eu^{2+} ion and indicative of weak anisotropy. Below T_N, a significant anisotropy of $\chi_\perp/\chi_{//} \approx 2.3$ develops, consistent with A-type magnetic order as observed in isostructural analogs and as predicted by the density functional theory calculations reported herein. The positive Weiss temperatures of θ_W=19.2 K for $\mu_0 H \perp c$ and θ_W=41.9 K for $\mu_0 H // c$ show a similar anisotropy and suggest competing ferromagnetic and antiferromagnetic interactions. Comparing Eu magnetic ordering temperatures across trigonal EuM_2X_2 (M=divalent metal, X=pnictide) shows that $EuZn_2P_2$ exhibits the highest ordering temperature, with variations in T_N correlating with changes in expected dipolar interaction strengths within and between layers and independent of the magnitude of electrical conductivity. These results provide experimental validation of the crystochemical intuition that the cation Eu^{2+} layers and the anionic $(M_2X_2)^{2-}$ framework can be treated as electronically distinct subunits, enabling further predictive materials design.

Introduction: Zintl phase materials are known to exhibit various phenomena including topological insulators, Dirac semimetals, colossal magnetoresistance, anomalous Hall effect, and spin Hall effect, with applications ranging from thermoelectricity, superconductivity, catalysis, spintronics, optoelectronics, and solar cells.[1-15] Zintl phases typically consist of a strongly covalently bonded anionic framework with separate cations to provide charge balance. Due to this difference in bonding types, the cationic and anionic subunits can often be tuned or modified independently, enabling systematic materials design of phenomena that requires precise tuning of multiple factors simultaneously.[14] A recent example of the success of this tunability is the discovery of magnetic topological insulators in $EuIn_2As_2$ and $MnBi_2Te_4$, where the electronic structure of the anionic framework provides the topology, while the magnetic order comes from distinct electrons on the cations.[1,6,16]

When the cationic framework is constructed of magnetic ions and the anionic framework is non-magnetic with a closed-shell electron configuration, Zintl phases can realize a variety of magnetic lattices and enable concrete comparisons to analytical theories.[17,18] Further, adjusting the electronic structure of the anionic framework with a fixed cationic lattice enables determination of the key interaction pathways within and between structural subunits, critical knowledge needed to discover and engineer novel electronic and magnetic phases.

More concretely, layered, insulating, Eu-based EuM_2X_2 (M=metal, X=pnictide) Zintl compounds provide realizations of weakly coupled square or triangular magnetic lattices, depending on the preferred geometry of the M_2X_2 layer ($ThCr_2Si_2$-type or anti-La_2O_3-type respectively). The half-filled, L=0 nature of Eu^{2+} (J=S=7/2) ensures minimal effects from local crystal fields (single ion anisotropy). In such materials, Eu can be partially or fully substituted with Ba, Sr, and/or Ca to dilute the magnetic lattice while holding the overall unit cell parameters constant. Alternatively, the anionic framework can be adjusted to change the cation ion separation and hence strength of the magnetic interactions within or between cationic layers. By adjusting the electronic structure of the anionic framework, the degree of interaction screening (or enhancement due to, e.g., superexchange or RKKY interactions) is also variable.

In this work, we report the physical properties of $EuZn_2P_2$ single crystals prepared via flux growth, and provide comparisons to other members of the family. Single-crystal x-ray diffraction at T=213 K confirms the previously reported $CaAl_2Si_2$ structure type, with triangular Eu^{2+} layers separated by $(Zn_2P_2)^{2-}$ layers of edge-sharing tetrahedra.[18] Bulk resistivity measurements reveal insulating behavior with an estimated activation energy of E_g=0.11eV. Specific heat measurements reveal a lambda anomaly at T_N = 23 K, with a broad hump continuing down to T=2 K. After fitting a phonon model to T > 25 K, the estimated integrated change in recovered magnetic entropy is ΔS_{mag}=11.3 Jmol^{-1}K^{-1} from T=0 K to T=T_N, close to ⅔ of the total entropy recovered for S=7/2 ions, ΔS_{mag}=Rln(8). Magnetization measurements show a cusp at T_N=23 K, indicative of the formation of Eu antiferromagnetic order. Above T_N, Curie-Weiss analysis yields p_{eff}=8.61 for $\mu_0H\perp$c and p_{eff}=7.74 for μ_0H//c, close to the expected value for $4f^7$ J=S=7/2 Eu^{2+} ions (p_{eff}=7.94). Below T_N, a significant anisotropy of $\chi_\perp/\chi_{//}\approx2.3$ develops, consistent with A-type magnetic order as observed in isostructural analogs. The positive Weiss temperatures of θ_W=19.2 K for $\mu_0H\perp$c and θ_W=41.9 K for μ_0H//c show a similar anisotropy, and suggest competing ferromagnetic and antiferromagnetic interactions. Density functional theory (DFT) calculations recapitulate the insulating behavior and predict A-type Eu magnetic order, in agreement with our observations. Overall, such results allow us to expand our knowledge in the chemical perspectives in the nature of magnetism in Eu-based Zintl compounds and its correlation to the electrical conductivity.

Methods: Single crystals of $EuZn_2P_2$ were synthesized using elemental Eu (ingot, Yeemeida Technology Co., LTD 99.995%), Zn (shots, Sigma-Aldrich 99.99%), red P (Sigma-Aldrich 97+%), and Sn (shots, Sigma-Aldrich 99.99%). The elements were put in a 1:2:2:45 ratio and a total mass of 5 grams were put in a Canfield crucible (size: 2mL). Zn and Sn were placed in the crucible at atmospheric conditions, while Eu and P were added later in an Ar-filled glove box. The Canfield crucible was placed in a quartz ampoule with quartz wool below and above the crucible, evacuated, and sealed under 1.2×10^{-2} torr of pressure. The evacuated ampoules were loaded in a box furnace at an angle of 45º. The temperature was ramped at rate of 100ºC/h to T=500 ºC for 4 hours. This step allowed for Sn flux to be in a liquid state. The furnace was then ramped from T=500ºC to T=1150ºC at the rate of 100ºC/hr and held for 24 hr. The furnace was then slowly cooled to T=850ºC at the rate of 5ºC/hr, then removed hot, inverted, and immediately centrifuged. Centrifugation took 2-3 minutes. Hexagonal plate-like crystals of size 3 mm along the long direction were removed from the frit. These single crystals of $EuZn_2P_2$ were found to be stable in air over period of months.

Powder x-ray diffraction (XRD) data, used to confirm phase purity of the single crystals, were collected over an angle range of 5°–60° on a laboratory Bruker D8 Focus diffractometer with a LynxEye detector and Cu Kα radiation. Single-crystal x-ray data were collected on a Bruker-Nonius X8 Proteum (Mo Kα radiation) diffractometer equipped with an Oxford cryostream. Integration and scaling were performed using CrysalisPro (Version 1.171.39.29c, Rigaku OD, 2017). A multiscan absorption correction was applied using SADABS.[19] The structure was solved by direct methods, and successive interpretations of difference Fourier maps were followed by least-squares refinement using SHELX and WinGX.[20,21]

Magnetization data were collected on a Quantum Design Magnetic Property Measurement System (MPMS). Magnetic susceptibility was approximated as magnetization divided by the applied magnetic field ($\chi \approx M/H$). To account for shape effects, a demagnetization correction was incorporated, with N=0.76 for $\mu_0 H$//c and N=0.18 for $\mu_0 H \perp$c. In addition, heat capacity data were collected on a Quantum Design Physical Properties Measurement System using the semiadiabatic method and a 1% temperature rise.

The resistivity measurements were performed in a Quantum Design Physical Property Measurement System (PPMS) using a Lake Shore Model 372 AC Resistance Bridge. An AC current set to autorange between 10nA - 1μA with an excitation frequency of 13.7 Hz was applied. The measurement was performed on a crystal with a four-probe configuration consisting of platinum wires and Epo-Tek silver epoxy H20E-FC. The picture of the single crystal with the Pt leads can be found in Figure 6a.

Density functional theory (DFT) based first principles calculations were performed using the projector augmented-wave (PAW) method as implemented in the VASP code.[22,23] We used the PBE exchange-correlation functional as parametrized by Perdew-Burke-Ernzerhof.[24,25] For the self-consistent calculations a Monkhorst-Pack k-mesh of size 15×15×5 was used to sample the Brillouin zone (BZ). The energy cutoff is chosen 1.5 times as large as the values recommended in relevant pseudopotentials. Spin-orbit coupling (SOC) was included self-consistently. The Eu 4*f* states were treated by employing the GGA+U approach with the U value set to 5.0 eV. Our calculations do not consider the effect of spin-orbit coupling (SOC), which is expected to be too weak to significantly affect the band gaps and exchange couplings that are the focus of the present work. The Eu 4*f* electrons were treated differently in the nonmagnetic (NM) case, where we used a Eu pseudopotential with 4*f* electrons in the core.

Results and Discussion:

Structure: The single-crystal x-ray diffraction (SCXRD) data for $EuZn_2P_2$ at T=213 K are consistent with the previously reported structure with the trigonal space group, P-3m1.[26] A precession image along the (hk0) plane is shown in Fig. 1a. Tables 1, 2, and 3 provide the details, atomic coordinates and atomic displacement parameters of the final refinement, which converged to R1=1.04% and wR2=2.46%. The bond valence sum for Eu is 1.6+ implying that the Eu is divalent, i.e. Eu^{2+}.[26] As-grown crystals of $EuZn_2P_2$, Figure. 1b, were found to be phase pure via powder x-ray diffraction after cleaning the excess tin from surfaces. The Zintl structure of $EuZn_2P_2$, Figure. 1c, contains Eu^{2+} layers separated by an anionic framework of $[Zn_2P_2]^{2-}$ edge-sharing tetrahedra. The stacking of these layers forms an octahedral coordination environment for Eu^{2+}.

The structure of $EuZn_2P_2$ is a member of the La_2O_3 family, sometimes called the Ce_2O_2S type, and structurally written as $[La_2O_2]^{2+}O^{2-}$.[18,27] $EuZn_2P_2$ is formally of the anti-La_2O_3-type (more commonly known as the $CaAl_2Si_2$-type), with anionic $[Zn_2P_2]^{2-}$ layers and cationic Eu^{2+}. Looking beyond those containing Eu, this is a very common structure type, including binaries like Mg_3Sb_2 (Figure. 1d) ternaries such as Li_2MnO_2 (Figure. 1e) and quaternaries such as $NaLiCdS_2$ (Figure. 1f).[27-31] All these structures crystallize into the same P-3m1 space group rationalized by the Zintl concept where the cation donate their valence electrons to stabilize the anionic tetrahedral framework. In these structures, individual tetrahedra are polar – with an elongation along the stacking axis (c-axis). For example, in the case of $EuZn_2P_2$, one Zn-P bond being 2.5303(10) Å, but the three equivalent Zn-P bonds being 2.4608(3) Å. These units are arranged in an alternating up/down pattern so there is no net electric polarity even in a single layer. However, the anionic layers might be expected to have a significant electric quadrupolar response, something that appears to be uninvestigated to date and is worthy of future study.

Heat Capacity: As Eu magnetic order is expected, heat capacity measurements were carried out on $EuZn_2P_2$ single crystals from T=2-300 K to identify possible phase transitions. A lambda anomaly at T_N =23 K is observed, Figure. 2a, and, when combined with magnetization (vida infra), is indicative of Eu antiferromagnetic order. The overall shape of the transition – a sharp peak followed by a broad hump at lower temperatures, is commonly observed in S=7/2 magnets on simple-cubic-like lattices.[31] Extraction of the magnetic contribution to the specific heat is non-trivial, as the most direct non-magnetic structural analog would be $BaZn_2P_2$, which adopts the distinct $ThCr_2Si_2$ structure type, whereas others have large differences in molar masses relative to $EuZn_2P_2$.[32] We thus chose to construct a phonon model to fit the high temperature specific heat. The chosen model, the two Debye model is given by:

$$\frac{C_p}{T} = \frac{C_D(\theta_{D1}, s_1, T)}{T} + \frac{C_D(\theta_{D2}, s_2, T)}{T} \qquad (1)$$

$$\mathrm{C_D}(\theta_\mathrm{D}, \mathrm{T}) = 9\mathrm{sR}\left(\frac{\mathrm{T}}{\theta_\mathrm{D}}\right)^3 \int_0^{\theta_\mathrm{D}/\mathrm{T}} \frac{(\theta/\mathrm{T})^4 e^{\theta/\mathrm{T}}}{[e^{\theta/\mathrm{T}}-1]^2} \, \mathrm{d}\frac{\theta}{\mathrm{T}} \qquad (2)$$

Where θ_{D1} and θ_{D2} are the Debye temperatures, s_1 and s_2 are the oscillator strengths, and R is the molar Boltzmann constant. When fitting phonons in heat capacity, we commonly fit using a Debye and Einstein models which correspond to acoustic and optic phonons. In the $EuZn_2P_2$ single crystals, a single Debye model was not sufficient to fit the experimental data. The Einstein model could not incorporate because the was no T_{max} in the C_p/T^3 versus T plot (not shown in the manuscript). Therefore, we tried a combination of two Debye models, which not only fitted the experimental data well but also gave physical oscillator terms that added up to the total number of atoms in the formula unit. The fit and physical oscillator terms made for criteria for our choice of two Debye models. It is physically motivated by the distinct subunits: the phonon modes of the anion framework are expected to be distinct, energetically, from those arising from the cationic lattice, and is commonly observed in complex materials.[14,32,33] The model parameters from the least-squares refinement to the data for T>25 K, are given in Table 4. The total oscillator strength s_1+s_2 = 5.18(6). This is in good agreement with the expected value of 1+2+2 = 5, the total number of atoms per formula unit in $EuZn_2P_2$.

After subtracting this phonon contribution, the sample heat capacity from T=2-300K was integrated to determine the change in entropy corresponding to magnetic order in $EuZn_2P_2$. Figure. 2b shows that the change in the magnetic entropy reaches a maximum of ΔS_{mag}=11.3 J.mol^{-1}.K^{-1} just above T_N. A compound that consists of Eu^{2+} without any multivalence of Eu or other magnetic ions should have a recovery of entropy ΔS_{mag}=Rln(8)=17.3 J.mol^{-1}.K^{-1}, so the observed value is ~⅔ of that expected. The most likely explanation is that the two Debye model is over-estimating the phonon contribution, particularly in the region just above T_N, as a gradual continued entropy recovery is expected for S=7/2 beyond T_N.[31] We also attribute the factor of ~⅔ to some magnetic fluctuations generated from the trigonal lattice, which is known in some cases to host a classical spin liquid.[34] The unphysical dip of the integrated ΔS_{mag} above T_N in Figure. 2b is consistent with this possibility. However, another possibility that cannot be ruled out is that there is additional entropy below T= 2K that is not captured by a linear extrapolation of Cp/T approaching 0 at T=0 K. One cannot completely rule out artifacts and the presence of magnetic entropy beyond the phonon subtraction region, thus the heat capacity analysis was some considerations and limitations.

Magnetization: Magnetization measurements provide details on the type of magnetic order in $\mathrm{EuZn_2P_2}$ and enable determination of the magnetic phase diagram. Temperature-dependent magnetic susceptibility, measured with an applied field perpendicular and parallel to the layers (c axis), Figures. 3a and 3b, show a clear antiferromagnetic phase transition at T_N=23K. The data from T=75-300K for $\mu_0 H\perp$c and T=150-300 K for $\mu_0 H$//c are well described by the Curie-Weiss law:

$$\chi = \frac{C}{T-\theta_w} + \chi_0 \qquad (3)$$

Where χ_0 is the temperature independent susceptibility, C is the Curie constant, and θ_W is the Weiss temperature. The fits are shown in Figure 3d and 3e and the best least-squares parameters are given in Table 5. The p_{eff} extracted from the Curie constants are 8.61 for $\mu_0 H\perp$c and 7.75 for $\mu_0 H$//c, are consistent with the theoretical p_{eff} =7.94 for Eu^{2+}. The positive Weiss constants indicate dominant ferromagnetic interactions; in combination with the observed antiferromagnetic order, this implies a mixture of magnetic exchange interactions. Another noticeable feature, in the susceptibility data is the anisotropy in $\mu_0 H\perp$c and $\mu_0 H$//c, Figure 3c and 3f. The anisotropy is larger below the T_N in comparison to above the T_N with $\chi_\perp/\chi_{//}$ in the range 0.8-1.25 above T$_{\mathrm{N}}$, rising rapidly below T_N to $\chi_\perp/\chi_{//}$~2.3 at T=2K. This anisotropy is not due to demagnetization – which has been corrected for in these data – and instead implies spin alignment in the ab plane below T_N. This is in agreement with observations on related Eu compounds.[36-39]

To further evaluate the magnetic behavior, $M(H)$ curves were collected as a function of temperature for both $\mu_0 H\perp$c and $\mu_0 H$//c, Fig. 4a and 4b. In both crystal directions, the magnetization saturates at 7μ_B, the expected value for divalent Eu^{2+}. This saturation rules out any Eu^{2+}/Eu^{3+} mixed valency in $\mathrm{EuZn_2P_2}$. The highly linear $M(H)$ behavior before saturation in both directions is common to many Eu^{2+} materials. [36-39] However, there are noticeable differences in the $M(H)$ data in the $\mu_0 H\perp$c and $\mu_0 H$//c directions. The saturation of 7μ_B happens at different magnetic fields, which implies that there is a difference in the magnetic stiffness in the two directions. These anisotropic features are consistent with the susceptibility results in Figure. 3a-f. It takes little applied magnetic field ($\mu_0 H$=0.75 T) to fully polarize the spins in the $\mu_0 H$//c direction in comparison to the $\mu_0 H\perp$c direction ($\mu_0 H$=2.25 T). This behavior implies a higher anisotropy in plane than out of plane and no signs of spin glass behavior. The θ_w is usually attributed to ferromagnetic interactions. However, from $M(T)$ we observe that the overall magnetic order is most definitely antiferromagnetic (the sharp peak is attributed to T$_{\mathrm{N}}$). However, if we look at individual Eu layers, it is apparent that the Eu atoms within a plane are ferromagnetically coupled to one another (i.e., the intra-layer interaction is ferromagnetic), whereas each layer is antiferromagnetically coupled to adjacent layers (i.e., the inter-layer interaction is antiferromagnetic). The positive θ_w is indicative of dominance of ferromagnetic interactions (coming from intra-layer interactions which is ferromagnetic layers) over the antiferromagnetic layers (inter-layer interactions). Another feature is that the Eu spins in the $EuZn_2P_2$ do not undergo any apparent phase transitions as a function of field and smoothly transition into the field polarized state. To extract the characteristic fields associated with these behaviors, Figures. 4c and 4d show the derivative as a function of the field.

Figure. 5a and 5b show the critical fields in M(H) as a function of field direction. From the M(T) measurements in Figure 3a and 3b, we know that $EuZn_2P_2$ is net antiferromagnetic. The Eu spins then reorient themselves to a field polarized paramagnetic/ferromagnetic state on applying a sufficiently large magnetic field. These data are sufficient to identify the type of magnetic order present: as described above, the spins lie in the ab plane. The order cannot be G-type (all antiferromagnetic within and between Eu layers), since in that case a proper phase transition should be observed with an applied field. The triangular lattice within each layer makes C-type order (ferromagnetic between layers, antiferromagnetic within layers) unlikely as there is no evidence of a structural phase transition. Further, with C-type order one would expect a field-driven magnetic transition along one of the two directions, while none are observed. We are thus left with A-type order (ferromagnetic layers stacked antiferromagnetically) as the prime candidate for the magnetic order. Such an order can continuously rotate to a field polarized state independent of the applied field direction, in agreement with the data here. It is also in agreement with the known magnetic order in isostructural analogs.[40-43]

Resistivity: To explore the electronic behavior, the temperature dependence of the electrical resistivity was measured for T=140-400K, Figure 6a. The resistivity decreases with temperature in the paramagnetic state and the order of magnitude of the resistivity is 10^3 Ω.cm at T=300 K consistent with insulating behavior in $EuZn_2P_2$. In order to extrapolate the bandgap through the resistance, the Arrhenius model was fitted to the resistivity data as $ln(\rho/\rho_{T=400K})$ versus T^{-1} in Figure 6b. In the Arrhenius model, a linear trend explains that the resistivity follows an activation type relation, $\rho \propto e^{E_g/k_B T}$, and fits $EuZn_2P_2$ well over the range measured. The extracted bandgap is E_g=0.11 eV. We note that a recent conference proceedings claims to have observed similar behavior in $EuZn_2P_2$.[44]

Theory: DFT calculations were performed for all four simple magnetic configurations with spins in the ab plane: G-type, C-type, A-type, and all ferromagnetic (FM). The energies of FM, G-type AFM, and C-type AFM orders are found to be 1.75, 11.47, and 10.43 meV higher than the A-type AFM, which is lowest in energy, with the FM as a close second. Since G-type and C-type orders are much higher in energy, we did not include them in our considerations. The theory is thus in agreement with the magnetization measurements and provides further evidence of A-type order in $EuZn_2P_2$. In this case, the computed moments are $\pm 6.935\mu_B$ for the Eu, $\pm 0.005\mu_B$ for Zn, and $\pm 0.018\mu_B$ for the P, with no net moment on the Zn_2P_2 tetrahedra. DFT also predicts $EuZn_2P_2$ to be an electrical insulator in the antiferromagnetic state. This insulating behavior persists in the FM configuration, Figure 7b, and implies that $EuZn_2P_2$ should be an insulator at all temperatures, in agreement with experiment (we note that the gap for comparison to theory is 2Eg as defined here, i.e. 0.22 eV). The computed magnetic moments do change slightly in the FM case, becoming $6.930\mu_B$ for the Eu, $-0.007\mu_B$ for Zn and $-0.027\mu_B$ for the P, with a total moment on the tetrahedra of $-0.066\mu_B$.

These calculations also demonstrate how the distinct subunits of a Zintl phase couple: the direct bandgap at Γ is E_g=0.60 eV in the antiferromagnetic configuration and E_g=0.48 eV in the ferromagnetic configuration (a 20% change), and the indirect bandgap from Γ to M is E_g=0.48 eV in the antiferromagnetic configuration and E_g=0.30 eV in the ferromagnetic configuration (a 38% change). The large change in activation energy occurs even though the states at the top of the valence band and the bottom of the conduction band are derived from the non-magnetic Zn and P atoms (and not Eu) – Eu 4*f* states are 1.2 eV below the valence band maximum in both cases. Figure 8 and Table 6 describe the shift in the activation energy as a function of *U*. While it is possible that the observed resistivity changes may arise from defect levels in the charge gap, they are also qualitatively consistent with the changes of gap seen in the DFT calculations

Given the impact of the Eu magnetism on the electronic structure of the Zn_2P_2 framework, it is natural to ask if the reverse is true – does the electronic structure of the anion framework significantly impact the magnetic order of the Eu lattice? To address this question, Table 7 gives key parameters for a set of isostructural EuM_2X_2 (M = metal, X = pnictide) magnets, including intra- and inter- layer distances, and room temperature resistivities. Note that in all cases, an insulating band structure (with either a positive or negative – i.e. semimetal – gap) is expected on the basis of electron count and bonding. Several trends are immediately apparent. First, $EuZn_2P_2$ has a higher Eu ordering temperature than any other known member of this family. Second, for a given metal M, the materials become more conductive and have a lower Eu ordering temperature as X increases down the pnictogen column. The magnitudes of the changes, however, are not uniform for different M. Given the large J=S=7/2 for Eu^{2+}, if the Eu-Eu interactions are primarily dipolar in nature, then one expects the magnetic interaction strength, and hence T_N, to scale as $1/d^3$, where d is the interion separation. We note that this holds even if the M_2X_2 layers screen or enhance a portion of the dipolar interaction, as would be expected in general when the magnetic permeability is not exactly unity.[52] Simply using the intralayer or interlayer distances combined with number of nearest neighbors gives partial trends, but does not unify the observations across different choices of M. We thus applied a multilinear regression to determine if some linear combination of $1/d_{nn}^3$ (d_{nn} = intralayer Eu-Eu distance) and $1/d_{il}^3$ (d_{il} = interlayer Eu-Eu distance) could explain all the data in Table 7. This yielded coefficients close to a 1:-4 ratio. Fixing the combination at exactly this ratio yields the trend in Figure 9, which shows a monotonic dependence of T_N on this mixture of Eu-Eu distances across different choices of M. This relationship holds across five orders of magnitude of conductivity, and demonstrates a dipolar-like scaling of the Eu-Eu interactions and suggests that the primary effect of the anionic framework is to modulate a dipolar interaction via changes in Eu-Eu distances (rather than, e.g., being due to superexchange or RKKY interactions which should be weak, and would not scale as $1/d^3$).[53] The observed ratio of 1:-4 is also consistent with the structure. The full expression for the magnetic dipolar interaction energy is $= -\frac{\mu_0}{4\pi r^3}[3(m_1 \cdot \hat{r})(m_2 \cdot \hat{r}) - m_1 \cdot m_2]$. Depending on the orientation of the dipole moments (m_1, m_2) relative to the vector connecting the two dipolar sites ($\hat{r}$), the interaction can favor either ferromagnetic (when they are coparallel) or antiferromagnetic (when they are perpendicular) alignments. Thus, the sign of a dipolar magnetic interaction can be either positive or negative. From the observed order – in-plane ferromagnetic layers aligned antiferromagnetically -- we expect the nearest neighbor interaction and the between-layer interaction to be opposite in sign, in agreement with the model (1 and -4). The magnitude of the coefficients, however, cannot just be extracted from the number (and relative distances) of nearest neighbors, because it also depends on the local magnetic permeability within versus between Eu layers, and also must account for (in an effective fashion) the longer range dipolar interactions – the next nearest neighbor in-plane interactions are about the same distance as the interlayer Eu-Eu ions for example. Further studies are necessary to determine whether this dipolar-like scaling arise from true dipolar interactions or other interactions manifesting in net as dipolar.

Conclusion: $EuZn_2P_2$ single crystals prepared via a flux technique crystallize in the trigonal anti-La_2O_3 ($CaAl_2Si_2$) structure type and exhibit Eu antiferromagnetic order at T_N= 23 K. Heat capacity results showed a change in the magnetic entropy saturation at ~⅔Rln(8) likely limited by the available phonon contribution model. Via magnetic susceptibility measurements the anisotropy of the $\mu_0H\perp c$ and $\mu_0H//c$ directions of $EuZn_2P_2$ single crystals was characterized. A significant anisotropy develops below T_N. The magnetic phase diagram allows identification of the magnetic structure of $EuZn_2P_2$ as A-type magnetic order. Resistivity measurements indicate insulating behavior with an experimental bandgap of E_g=0.11 eV, consistent with DFT calculations. Comparisons amongst related materials shows that the dominant effect of the anionic framework on the Eu lattice magnetism scales as expected for magnetic dipolar interactions. Overall, our results help us gain insights into the polyanionic contributions to the conductivity and magnetism in the EuM_2X_2 structures. For future work, local probes to understand the local coordination environment in $EuZn_2P_2$ would allow understanding of the structural coordination and high resistance measurements to understanding the conductivity close to Neél temperature to evaluate the conduction pathways in $EuZn_2P_2$.

Acknowledgments: The authors would like to thank M. Siegler for technical assistance. This work was supported as part of the Institute for Quantum Matter and Energy Frontier Research Center, funded by the U.S. Department of Energy, Office of Science, Office of Basic Energy Sciences, under Award DE-SC0019331. The MPMS was funded by the National Science Foundation, Division of Materials Research, Major Research Instrumentation Program, under Award 1828490.

References:

1. Y. Xu, Z. Song, Z. Wang, H. Weng, X. Dai, Higher-order topology of the axion insulator $EuIn_2As_2$. *Phys. Rev. Lett.* **122**, 256402 (2019).
2. P. Rosa, Y. Xu, M. Rahn, J. Souza, S. Kushwaha, L. Veiga, A. Bombardi, S. Thomas, M. Janoschek, E. Bauer, M. Chan, Z. Wang, J. Thompson, N. Harrison, P. Pagliuso, A. Bernevig, F. Ronning, Colossal magnetoresistance in a nonsymmorphic antiferromagnetic insulator. *npj Quantum Mater*. **5**, 52 (2020).
3. L. Z. Sun, A. F. Wang, H. M. Mu, H. H. Wang, Z. F. Wang, T. Wu, Z. Y. Wang, X. Y. Zhou, and X. H. Chen, Field-induced metal-to-insulator transition and colossal anisotropic magnetoresistance in a nearly Dirac material $EuMnSb_2$. *npj Quan. Mat.*, **6**(1), 1-8 (2021).
4. J. Yan, Z. Z. Jiang, R. C. Xiao, W. J. Lu, W. H. Song, X. B. Zhu, X. Luo, Y. P. Sun, and M. Yamashita. Field-induced topological Hall effect in antiferromagnetic axion insulator candidate $EuIn_2As_2$. *Phys. Rev. Research.* **4**, 1, 013163 (2022).
5. J. Shuai, J. Mao, S. Song, Q. Zhang, G. Chen, Z. Rena, Recent progress and future challenges on thermoelectric Zintl materials. *Mater. Today Phys.* **1**, 74–95 (2017).
6. N. Varnava, T. Berry, T. M. McQueen, D. Vanderbilt, Engineering magnetic topological insulators in $Eu_5M_2X_6$ Zintls. *arXiv preprint* 2203.06212 (2022).
7. C. Chen, W. Xue, S. Li, Z. Zhang, X. Li, X. Wang, Y. Liu, J. Sui, X. Liu, F. Cao, Z. Ren, C.-W. Chu, Y. Wang, Q. Zhang, Zintl-phase Eu_2ZnSb_2: a promising thermoelectric material with ultralow thermal conductivity. *Proc. Natl Acad. Sci.* **116**, 2831 (2019).
8. T. F. Fässler, C. Kronseder, BaSn,: A Superconductor at the Border of Zintl Phases and Intermetallic Compounds. Real-Space Analysis of Band Structures. *Angew. Chem., Int. Ed. Engl.*, **36**, 2683 (1997).
9. K. L. Hodge, J. E. Goldberger, Transition metal-free alkyne hydrogenation catalysis with $BaGa_2$, a hydrogen absorbing layered zintl phase. *J. Am. Chem. Soc.* **141**, 19969–19972 (2019).
10. Z. Zada, A. Laref, G. Murtaza, A. Zeb, A. Yar, First-principles calculations of electronic and magnetic properties of XMn_2Y_2 (X = Ca, Sr; Y = Sb, Bi) compounds *Int. J. Mod. Phys. B.* **33**, 1950199 (2019).
11. Z. Zada, H. Ullah, R. Zada, S. Laref, A. Azam, S. Khan, A. A. Irfan, Structure stability, half metallic ferromagnetism, magneto-electronic and thermoelectric properties of new zintl XCr_2Bi_2 (X=Ca, Sr) compounds for spintronic and renewable energy applications. *Physica B: Con. Mat.*, **607**, 412866, 0921-4526 (2021).
12. A. Khan, A. H. Reshak, Optoelectronic and transport properties of Zintl phase $KBa_2Cd_2Sb_3$ compound. *Comput. Mater. Sci.* **95**, 328 (2014).
13. M. Kumar, N. Umezawa, W. Zhou, M. Imai, Electronic states of Zintl-phase solar-cell material $BaSi_2$ *J. Mater. Chem. A*, **5**, 25293 (2017).
14. T. Berry, S. R. Parkin, T. M. M. McQueen, Antiferro-and metamagnetism in the S=7/2 hollandite analog $EuGa_2Sb_2$. *Phys. Rev. Mat.*, **5**, 11, 114401 (2021).
15. K. P. Devlin, J. Zhang, J. C. Fettinger, E. S. Choi, A. K. Hauble, V. Taufour, R. P. Hermann, S. M. Kauzlarich, *Inorg. Chem.* **60**, 5711 8, (2021).
16. D. Zhang, M. Shi, T. Zhu, D. Xing, H. Zhang, J. Wang, Topological axion states in magnetic insulator $MnBi_2Te_4$ with the quantized magnetoelectric effect. *Phys. Rev. Lett*. **122**, 206401 (2019).

17. S. Bobev, E. D. Bauer, J. D. Thompson, J. L. Sarrao, G. J. Miller, B. Eck, R. Dronskowski, Metallic behavior of the Zintl phase $EuGe_2$: combined structural studies, property measurements, and electronic structure calculations. *J. Solid State Chem.* **177**, 3545 (2004).
18. C. Zheng, R. Hoffmann, R. Nesper, H. G. Von Schnering, Site preferences and bond length differences in $CaAl_2Si_2$-type Zintl compounds. *J. Am. Chem. Soc.***, 108** (8), 1876-1884 (1986).
19. R. C. Clark, J. S. Reid, The analytical calculation of absorption in multifaceted crystals. *Acta Cryst. A.* **51**, 887–897 (1995).
20. G. A. Sheldrick, Short history of SHELX. *Acta Cryst. A.* **64**, 112–122 (2008).
21. G. A. Sheldrick, SHELXT- Integrated space-group and crystal-structure determination. *Acta Cryst. A.* **71**, 3–8 (2015).
22. P. Hohenberg, W. Kohn, Inhomogeneous electron gas, *Phys. Rev.* **136**, 864–871 (1964).
23. W. Kohn, L. J. Sham, Self-consistent equations including exchange and correlation effects, *Phys. Rev.* **140**, 1133–1138 (1965).
24. G. Kresse, J. Furthmuller, Efficient iterative schemes for ab initio total-energy calculations using a plane-wave basis set, *Phys. Rev. B* **54**, 11169–11186 (1996).
25. G. Kresse, D. Joubert, From ultrasoft pseudopotentials to the projector augmented-wave method, *Phys. Rev. B* **59**, 1758–1775 (1999).
26. P. Klüfers, H. Neumann, A. Mewis, H. Schuster, AB_2X_2-Verbindungen im $CaAl_2Si_2$-Typ, VIII [1] / AB_2X_2 Compounds with the $CaAl_2Si_2$ Structure, VIII [1]. *Zeitschrift für Naturforschung B*, **35(10)**, 1317-1318 (1980).
27. W. C. Koehler, E. O. Wollan, Neutron-diffraction study of the structure of the A-form of the rare earth sesquioxides. *Acta Crystallographica***, 6,** 8-9, 741-742 (1953).
28. J. Zhang, L. Song, B. B. Iversen, Insights into the design of thermoelectric Mg_3Sb_2 and its analogs by combining theory and experiment. *Npj Comput. Mater.* **5,** 1, 76 (2019).
29. W. I. F. David, J. B. Goodenough, M. M. Thackeray, M. G. S. R. Thomas, The Crystal Structure of Li_2MnO_2. *Rev. Chim. Miner.***, 20**, 636-642 (1983**)**.
30. B. Deng, G. H. Chan, F. Q. Huang, D. L. Gray, D. E. Ellis, R. P. Van Duyne, J. A. Ibers, Synthesis, structure, optical properties, and electronic structure of $NaLiCdS_2$. *J. Solid State Chem.* **2007,** *180* (2), 759-764.
31. R. Lora-Serrano, D.J. Garcia, D. Betancourth, R.P. Amaral, N.S. Camilo, E. Estévez-Rams, L.A. Ortellado G.Z., P.G. Pagliuso, Dilution effects in spin 7/2 systems. the case of the antiferromagnet $GdRhIn_5$. *J. Magn. Magn. Mater.* **405**, 304–310 (2016).
32. T. Berry, L. A. Pressley, W. A. Phelan, T. T. Tran, T. M. McQueen, Laser-Enhanced Single Crystal Growth of Non-Symmorphic Materials: Applications to an Eight-Fold Fermion Candidate. *Chem. Mater.*, **32**, 5827-5834 (2020).
33. M. Sinha, H. K. Vivanco, C. Wan, M. A. Siegler, V. J. Stewart, E. A. Pogue, L. A. Pressley, T. Berry, Z. Wang, J. I. Johnson, M. Chen, T. T. Tran, W. A. Phelan, T. M. McQueen, Twisting of 2D Kagomé Sheets in Layered Intermetallics. *ACS Cent. Sci.*, **7**, 1381-1390 (2021).
34. Z. Zhu, P. A. Maksimov, S. R. White, A. L. Chernyshev, Topography of Spin Liquids on a Triangular Lattice. *Phys. Rev. Lett.*, **120**, 207203 (2018).
35. A. Balvanz, S. Baranets, M. O. Ogunbunmi, S. Bobev, Two Polymorphs of $BaZn_2P_2$: Crystal Structures, Phase Transition, and Transport Properties. *Inorg. Chem.* **60**, 18, 14426-14435 (2021).
36. V. K. Anand, D. C. Johnston, Metallic behavior induced by potassium doping of the trigonal antiferromagnetic insulator $EuMn_2As_2$. *Phys. Rev. B* **94**, 014431 (2016).
37. R. Rühl, W. Jeitschko, New pnictides with Ce_2O_2S-type structure. *Mater. Res. Bull.*, **14**, 513–517 (1979).

38. A. F. May, M. A. McGuire, D. J. Singh, R. Custelcean, G. E. Jellison, Structure and properties of single crystalline $CaMg_2Bi_2$, $EuMg_2Bi_2$, and $YbMg_2Bi_2$. *Inorg. Chem.* **50**, 11127–11133 (2011).
39. S. Pakhira, M. A. Tanatar, D. C. Johnston, Magnetic, thermal, and electronic-transport properties of $EuMg_2Bi_2$ single crystals. *Phys. Rev. B*, **101**, 214407 (2020).
40. J. Blawat, M. Marshall, J. Singleton, E. Feng, H. Cao, W. Xie, R. Jin, Unusual electrical and magnetic properties in layered $EuZn_2As_2$. *arXiv e-prints*, pp.arXiv-2202 (2022).
41. A. F. May, M. A. Guire, J. Ma, O. Delaire, A. Huq, R. Custelcean, Properties of single crystalline AZn_2Sb_2 (A=Ca, Eu, Yb). *J. Appl. Phys.* **111**, 033708 (2012).
42. I. Schellenberg, M. Eul, W. Hermes, R. A. Pöttgen, ^{121}Sb and ^{151}Eu Mössbauer spectroscopic investigation of $EuMn_2Sb_2$, $EuZn_2Sb_2$, $YbMn_2Sb_2$, and $YbZn_2Sb_2$. *Z. Anorg. Allg. Chem.* **636**, 85 (2010).
43. A. C. Payne, A. E. Sprauve, M. M. Olmstead, S. M. Kauzlarich, J. Y. Chan, B. A. Reisner, J. W. Lynn, Synthesis, magnetic and electronic properties of single crystals of $EuMn_2P_2$. *J. Solid State Chem.* **163**, 498 (2002).
44. Z. Bukowski, Magnetism, superconductivity and magnetotransport properties of Eu-based ternary pnictides. *Pedagogical University of Cracow*. 9788380846289 (2021).
45. T. Berry et al. Private Communication (2022).
46. Z. C. Wang, J. D. Rogers, X. Yao, R. Nichols, K. Atay, B. Xu, J. Franklin, I. Sochnikov, P. J. Ryan, D. Haskel, F. Tafti, Colossal magnetoresistance without mixed valence in a layered phosphide crystal. *Advan. Mat.*, **33**, 2005755 (2021).
47. A. Artmann, A. Mewis, M. Roepke, G. Michels, AM_2X_2-Verbindungen mit $CaAl_2Si_2$ Struktur. XI. Struktur und Eigenschaften der Verbindungen ACd_2X_2 (A:Eu, Yb; X: P, As, Sb). *Z. Anorg. Allg. Chem.* **622**, 679–682 (1996).
48. J.-Z. Ma, S.M. Nie, C.J. Yi, J. Jandke, T. Shang, M.Y. Yao, M. Naamneh, L.Q. Yan, Y. Sun, A. Chikina, V.N. Strocov, M. Medarde, M. Song, Y.-M. Xiong, G. Xu, W. Wulfhekel, J. Mesot, M. Reticcioli, C. Franchini, C. Mudry, M. Muller, Y.G. Shi, T. Qian, H. Ding, M. Shi, Spin fluctuation induced Weyl semimetal state in the paramagnetic phase of $EuCd_2As_2$. *Sci. Adv.* **5**, eaaw4718 (2019).
49. I. Schellenberg, U. Pfannenschmidt, M. Eul, C. Schwickert, R. A. Pöttgen, ^{121}Sb and ^{151}Eu Mössbauer spectroscopic investigation of $EuCd_2X_2$ (X = P, As, Sb) and $YbCd_2Sb_2$. *Z. f.ür anorganische und Allg. Chem.* **637**, 1863–1870 (2011).
50. H. Su, B. Gong, W. Shi, H. Yang, H. Wang, W. Xia, Z. Yu, P.-J. Guo, J. Wang, L. Ding, L. Xu, X. Li, X. Wang, Z. Zou, N. Yu, Z. Zhu, Y. Chen, Z. Liu, K. Liu, G. Li, Y. Guo, Magnetic exchange induced Weyl state in a semimetal $EuCd_2Sb_2$. *APL Mater.* **8**, 011109 (2020).
51. F. Wartenberg, C. Kranenberg, R. Pocha, D. Johrendt, A. Mewis, R. D. Hoffmann, B. D. Mosel, R. Pottgen, New Pnictides with the $CaAl_2Si_2$ Type Structure and the Stability Range of this Type *Z. Naturforsch., B: J. Chem. Sci.*, **57**, 1270–1276 (2002).
52. P. Hammond, Electric and Magnetic Images. Institution of Electrical Engineers Monograph No. 379 (1960).
53. D. C. Johnston, Magnetic dipole interactions in crystals. *Phys. Rev. B* **93**, 014421: 1–33 (2016).

Figure 1. (a) Single-crystal precession image of the (hk0) plane. **(b)** As-grown single-crystal of $EuZn_2P_2$. Structures of **(c)** $EuZn_2P_2$**, (d)** Mg_3Sb_2**, (e)** Li_2MnO_2, and **(f)** $NaLiCdS_2$ that crystallize in *P*-3m1 (164) and are anti-La_2O_3 ($CaAl_2Si_2$) structures containing 2D trigonal layers of cations separated by anionic layers of edge-sharing tetrahedra. The black box represents the unit cell in each case.[27.-31]

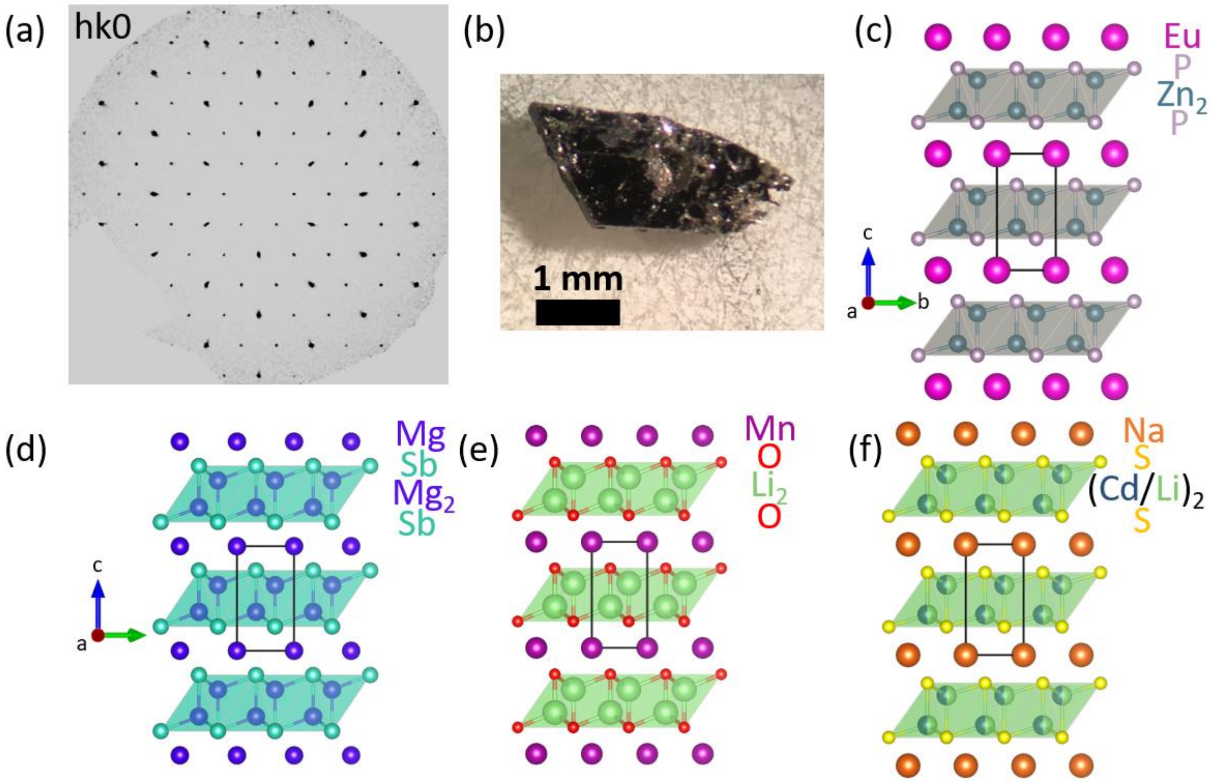

Figure 2. (a) Specific heat divided by temperature as a function of temperature for $EuZn_2P_2$ single crystals from T=2–300 K. The maroon filled squares denote experimental data, and the green is the phonons modeled using the Two-Debye model from T=30–300 K. The sharp transition at T=25 K is attributed to the antiferromagnetic phase transition. The bump around T=270 K is from Apiezon N grease used during the measurement. **(b)** The change in magnetic entropy was integrated after subtracting the phonons from T=2-300K. The ΔS_{mag} is close to ~2/3Rln(8). The light green in ΔSmag at around T=270 K is coming from Apiezon N grease.

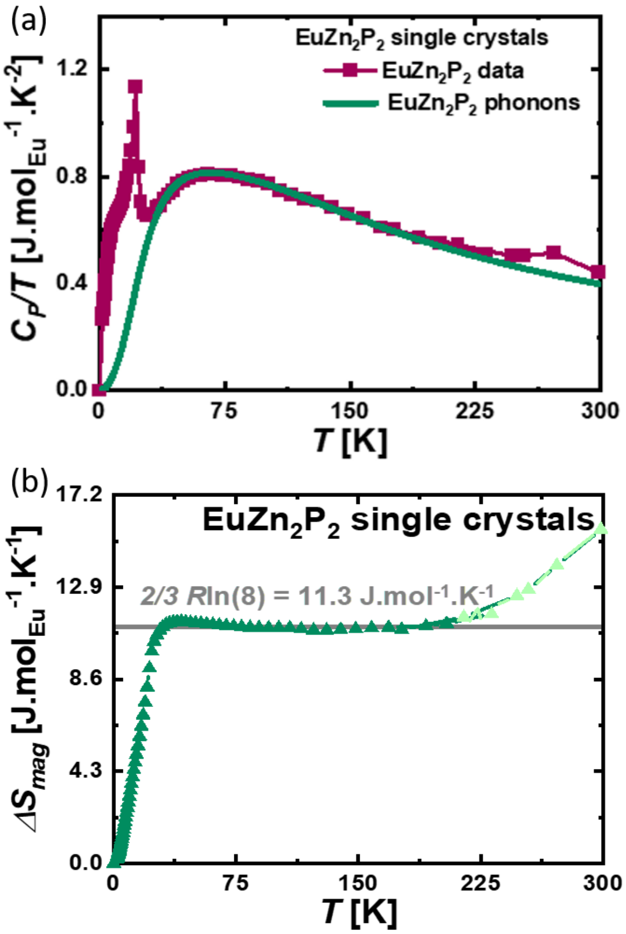

Figure 3. (a) Magnetization as a function of temperature with *μoH*||c and *μo*H = 0.1–7 T and *T*=2–300 K. The *μoH*=0.1 T data show a clear AFM transition at *T*=25 K, with a decrease in both sharpness of the transition and the temperature of the transition as the field increases. **(b)** Magnetization as a function of temperature *μoH*⊥c from *μoH*=0.1–7 T and *T*=2–300 K. The *μoH*=0.1 T data show a kink at *T*=25 K followed by an upturn, both of which are suppressed for *μoH*>0.1 T. **(c)** Comparison in the magnetization as a function of temperature, *μoH*⊥c and *μoH*||c, at *μoH* = 0.1 T over *T* =2–300 K. **(d)** Curie Weiss analysis for *μoH*||c from *μoH*=0.1 T in the range *T*=2–300 K, **(e)** Curie Weiss analysis *μoH*⊥c from μoH = 0.1 and *T*=2–300 K, and **(f)** ratio of magnetization *μoH*||c and *μoH*⊥c at *μoH*=0.1 T and *T*=2-300 K displaying the anisotropy below T_N .

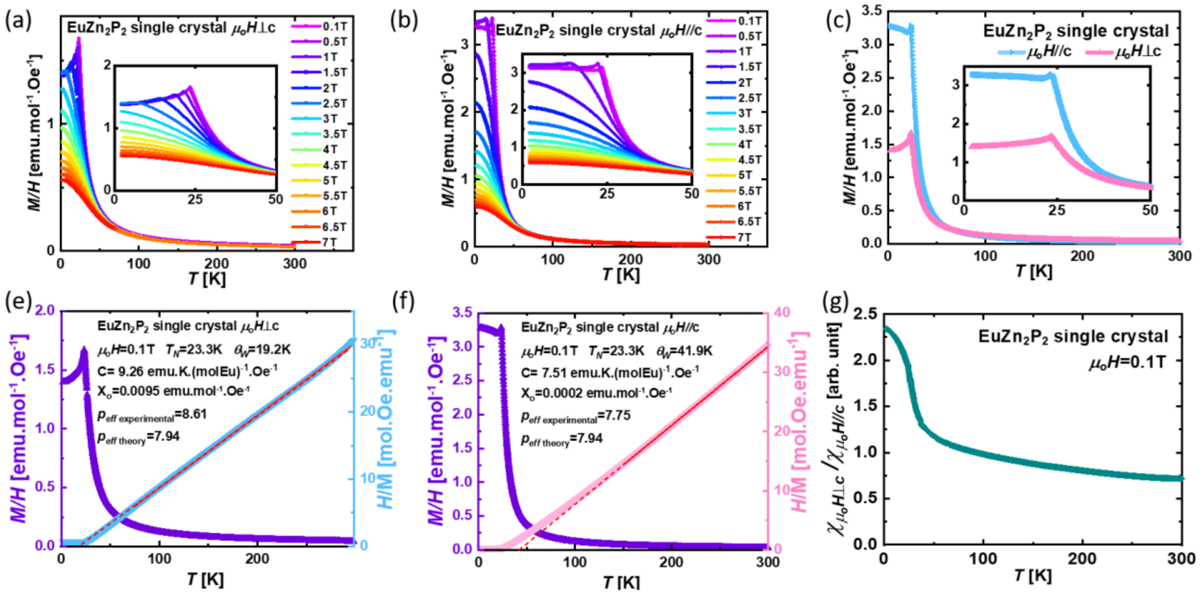

Figure 4. For each plot below, the following temperatures are shown: T = 2, 5, 8, 10, 20, 21, 100, and 300 K. **(a)** Magnetization as a function of magnetic field with $\mu o H \| c$ from $\mu o H = -7$ to 7 T; **(b)** Magnetization as a function of magnetic field with $\mu o H \perp c$ from $\mu o H = -7$ to 7; **(c)** derivative of magnetization over magnetic field as a function of magnetic field with $\mu o H \| c$; and **(d)** derivative of magnetization over magnetic field as a function of magnetic field with $\mu o H \perp c$.

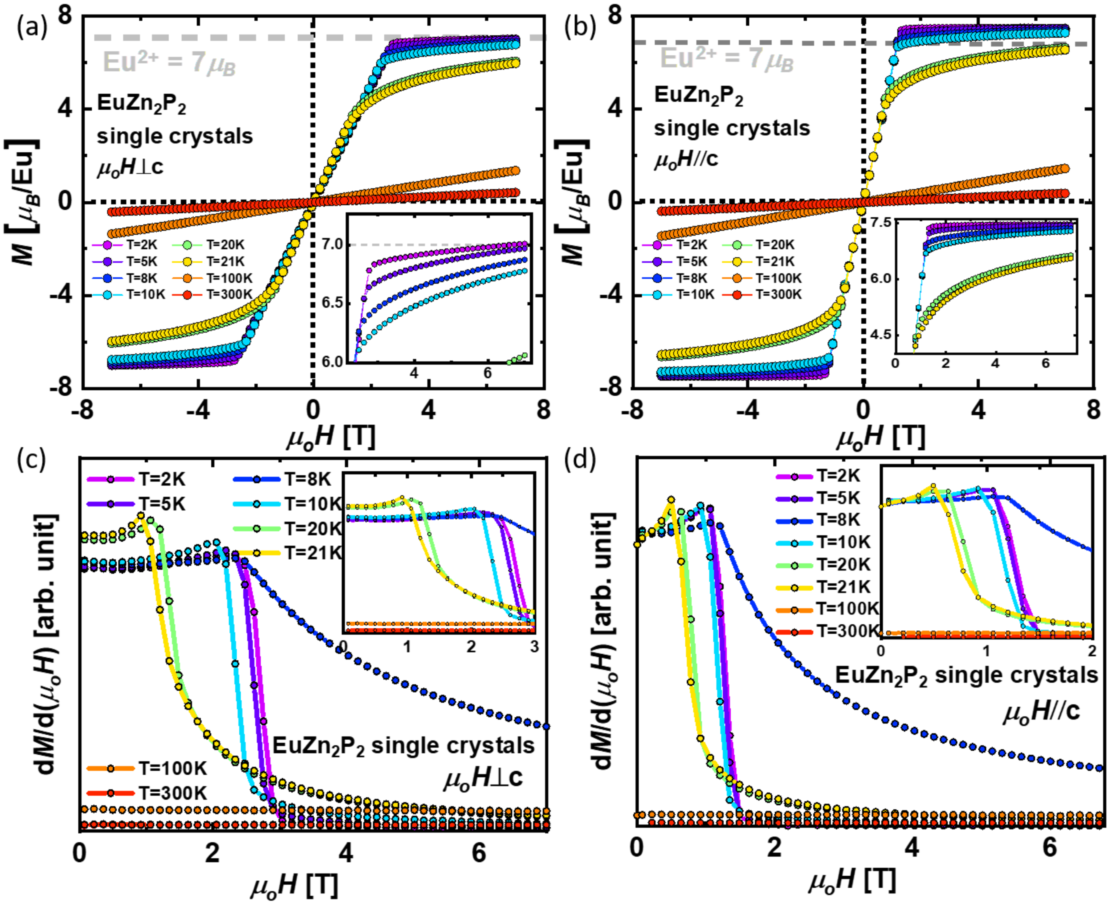

Figure 5. Magnetic phase diagram of $EuZn_2P_2$ with **(a)** $\mu o H \perp c$ and **(b)** $\mu o H || c$. In both cases, there is an anisotropic AFM state at low fields, followed by a PM state that continuously evolves to a field-polarized state. The transition from AFM to a field-polarized state was determined from the maximum in the M(T) data. **(c)** Proposed A-type antiferromagnetic structure of $EuZn_2P_2$.

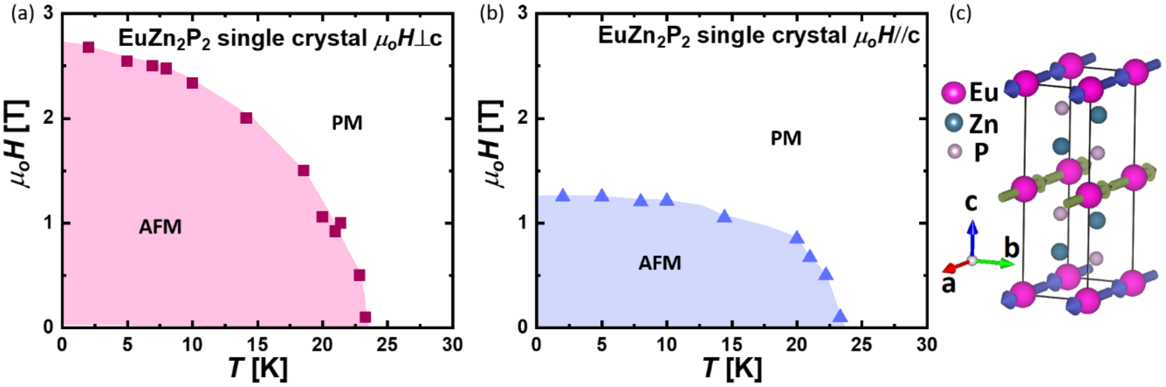

Figure 6. (a) Four probe resistivity data of $EuZn_2P_2$ single crystals at T=140-400K. **(b)** Natural logarithm of normalized resistivity as a function of $\frac{1}{T}$ measured on a single crystal of $EuZn_2P_2$ along the c-axis. The bandgap extrapolated is E_g=0.11eV and is fit to $ln\left(\frac{\rho}{\rho_{T=400K}}\right) = \frac{E_g}{k_B}\ \frac{1}{T}$.

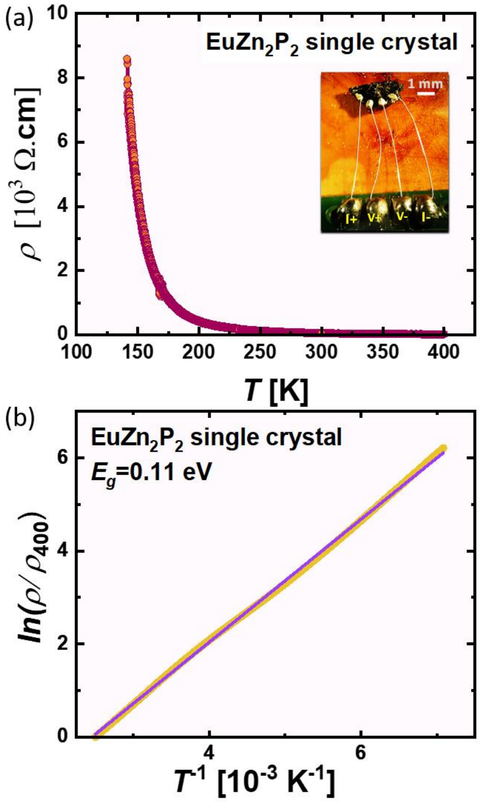

Figure 7. Density functional theory (DFT) calculation in the non-magnetic configuration **(a)-(c)**, ferromagnetic configuration (single unit cell) **(d)-(f)**, A-type antiferromagnetic configuration **(g)-(i)**, ferromagnetic configuration (doubled unit cell) **(j)-(l)**. For each case we present the unit cell, band structure, and the density of states.

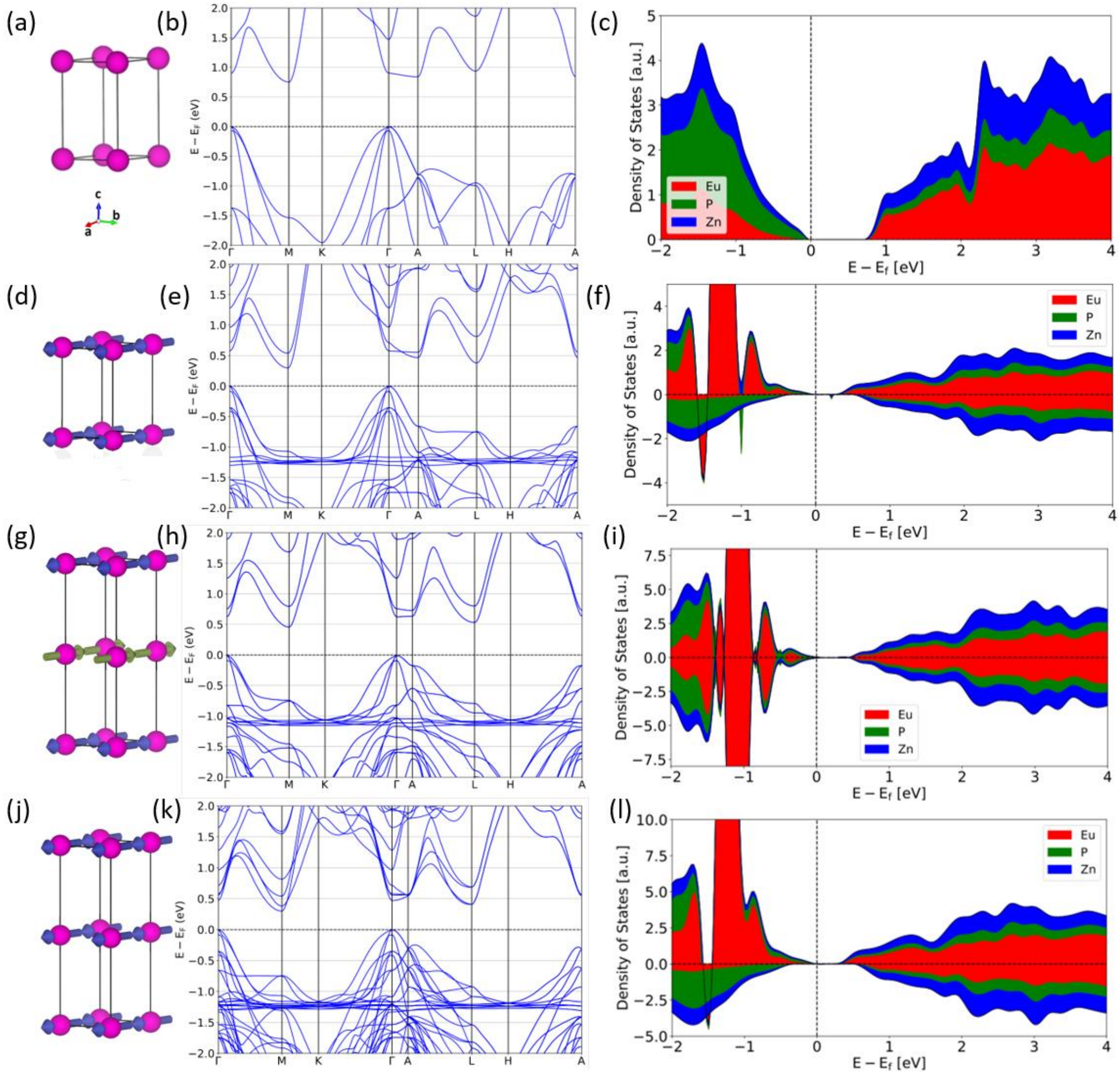

Figure 8. Density functional theory (DFT) band structure for the **(a-c)** FM and the **(d-f)** A-type AFM cases for U=4, 5, 6 eV. The plots below show sensitivity of activation energy with the value of U.

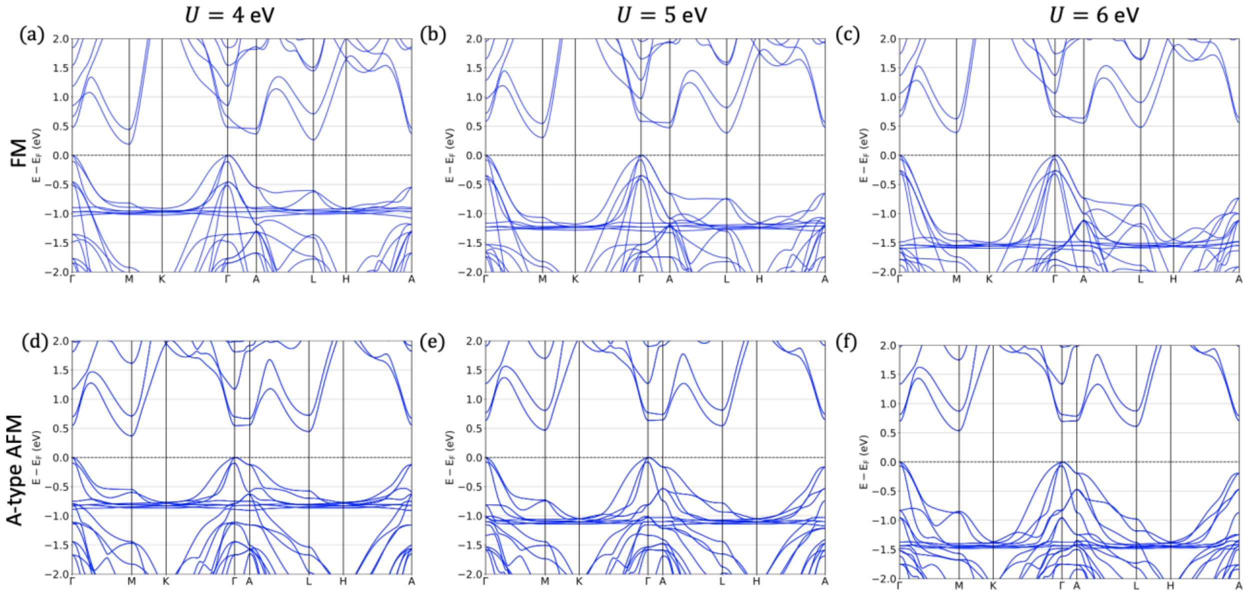

Figure 9. The Eu magnetic ordering temperature of EuM_2X_2 materials scales with the inverse cubed distance between intralayer and interlayer Eu-Eu ions within the cationic lattice implying dominate dipolar interactions.

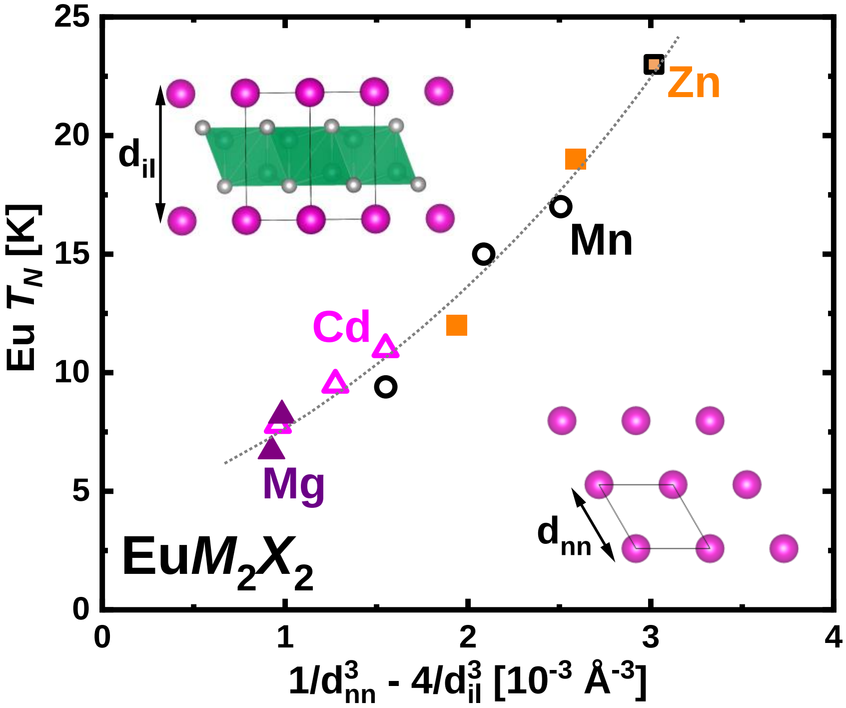

Table 1. Crystal data and refinement results for $EuZn_2P_2$

Formula	**$EuZn_2P_2$**
Crystal system	Trigonal
Space group	$P\bar{3}m1$ (No. 164)
FW (g/mol)	268.96
a (Å)	4.08497(18)
c (Å)	7.0019(4)
V ($Å^3$)	101.187(11)
Z	1
T (K)	213 (2)
Adsorption coefficient	27.612
Mo Kα (Å)	0.71073
Reflections collected / Number of parameters	180/10
Goodness of fit	1.188
$R[F]^a$	0.0104
$R_w(F_o^2)^b$	0.0246

[a] $R(F) = \Sigma||F_o| - |F_c||/\Sigma|F_o|$

[b] $R_w(F_o^2) = [\Sigma w(F_o^2 - F_c^2)^2/\Sigma w(F_o^2)^2]^{1/2}$

Table 2. Fractional atomic coordinates and isotropic displacement parameters based on the refined $EuZn_2P_2$ structure

Element	**Wyckoff Positions**	***x***	***y***	***z***	**Occupancy**	U_{iso}
Eu	1a	1	1	0	1	0.00674(10)
Zn	2d	2/3	1/3	0.36947(6)	1	0.00791(11)
P	2d	1/3	2/3	0.26915(12)	1	0.00637(16)

Table 3. Anistropic displacement parameters based on the refined $EuZn_2P_2$ structure

Element	**U_{11}**	**U_{22}**	**U_{33}**	**U_{23}**	**U_{13}**	**U_{12}**
Eu	0.00656(11)	0.00656(11)	0.00711(13)	0.000	0.000	0.00328(5)
Zn	0.00781(13)	0.00781(13)	0.0081(2)	0.000	0.000	0.00391(6)
P	0.0061(2)	0.0061(2)	0.0068(4)	0.000	0.000	0.00307(11)

Table 4. Fitting parameters to the C_p/T as a function of T for $EuZn_2P_2$ to extract the phonon contribution.

s_{D1} (oscillator strength/formula unit)	s_{D2} (oscillator strength/formula unit)	θ_{D1}(K)	θ_{D2}(K)
2.35(3)	2.83(3)	493(4)	182(3)

Table 5. Fitting parameters obtained by Curie Weiss analysis from magnetization data of $EuZn_2P_2$.

$EuZn_2P_2$	$\mu_0 H \perp c$	$\mu_0 H \parallel c$
Range [K]	150-300	150-300
C [emu.K.(mol Eu)$^{-1}$.Oe^{-1}]	9.26	7.51
θ [K]	19.2	41.9
χ_0 [emu^{-1}.(mol Eu).Oe]	0.0095	0.0002
p_{eff}	8.61	7.75

Table 6. Band gap extrapolated from U considerations at 4, 5, and 6 eV on the A-type AFM and FM cases corresponding to Figure 8.

U (eV)	A-type AFM Energy Gap (eV)	FM Energy Gap (eV)
4	0.3692	0.1904
5	0.4685	0.3027
6	0.5359	0.3901

Table 7. Key Eu lattice geometric parameters, observed magnetic ordering temperature, and room temperature resistivity, for a range of known EuM_2X_2 trigonal Zintl materials.

EuM_2X_2	**Interlayer Eu-Eu distance (Å)**	**Intralayer Eu-Eu distance (Å)**	**Eu T_N (K)**	**ρ_{ab} (mOhm-cm at T=300K)**	**References**
$EuZn_2P_2$	7.0019	4.0845	23	66	This Work
$EuZn_2As_2$	7.1810	4.2110	19	75	26,40
$EuZn_2Sb_2$	7.6090	4.4938	12	1.3	41,42
$EuMn_2P_2$	6.9936	4.1294	17	3.50×10^5	45
$EuMn_2As_2$	7.2250	4.2870	15	200	36
$EuMn_2Sb_2$	7.6740	4.5810	9.4	-	36,37
$EuCd_2P_2$	7.1790	4.3250	11	24	46,47
$EuCd_2As_2$	7.3500	4.4499	9.5	15	48,49
$EuCd_2Sb_2$	7.7230	4.6980	7.8	12	47,50
$EuMg_2Sb_2$	7.7240	4.6950	8.2	-	51
$EuMg_2Bi_2$	7.8483	4.7724	6.7	2.3	38,39